ACS Omega
http://pubs.acs.org/journal/acsodf
Article

g-C_3N_4 Nanosheet Supported CuO Nanocomposites for the Electrochemical Carbon Dioxide Reduction Reaction

Chien-Lin Sung,[§] Ren-Hung Wang,[§] You-Cheng Shih, Zhi-Ying Wu, Samuel R. Alvarado, Yu-Hsu Chang,* and Chia-Cheng Lin*

Cite This: ACS Omega 2023, 8, 7368−7377
Read Online

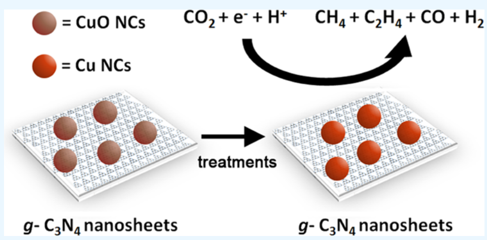

ABSTRACT: We have prepared CuO-derived electrocatalysts on a graphitic carbon nitride (g-C_3N_4) nanosheet support for the electrochemical carbon dioxide reduction reaction (CO_2RR). Highly monodisperse CuO nanocrystals made by a modified colloidal synthesis method serve as the precatalysts. We use a two-stage thermal treatment to address the active site blockage issues caused by the residual C18 capping agents. The results show that the thermal treatment effectively removed the capping agents and increased the electrochemical surface area. During the process, the residual oleylamine molecules incompletely reduced CuO to a Cu_2O/Cu mixed phase in the first stage of thermal treatment, and the following treatment in forming gas at 200 °C completed the reduction to metallic Cu. The CuO-derived electrocatalysts show different selectivities over CH_4 and C_2H_4, and this might be due to the synergistic effects of Cu-g-C_3N_4 catalyst−support interaction, varied particle sizes, dominant surface facets, and catalyst ensemble. The two-stage thermal treatment enables sufficient capping agent removal, catalyst phase control, and CO_2RR product selection, and with precise controls of the experimental parameters, we believe that this will help to design and fabricate g-C_3N_4-supported catalyst systems with narrower product distribution.

■ INTRODUCTION

The utilization of sustainable energy to alleviate the current dependence on fossil fuel-based energy sources is one of the solutions to address the emerging global warming and climate change. The intermittent nature of renewable energy sources nevertheless hinders the development of related techniques. Measures such as smart grids,[1] supercapacitors,[2] and electrochemical small molecule activations have been taken to address the issues. The electrochemical CO_2 reduction reaction (CO_2RR) offers an alternative route for renewable energy conversion and storage.[3] Among various CO_2RR products, hydrocarbons are more desired in consideration of energy density. Metallic electrodes have been used for CO_2RR, and Cu-based materials have especially drawn attention due to their unique catalytic performance for producing variable fuels.[4,5]

Efforts have been devoted to the development of Cu-based electrocatalysts to improve the CO_2RR catalytic activity and selectivity, such as CO_2RR with planar Cu,[6−9] Cu foams,[10] Cu_2O-derived catalysts,[11] CuO-derived nanoribbons,[12] CuO-derived microspheres,[13] CuO-derived nanowires,[13,14] plasma-treated Cu electrodes,[15] CuO-derived planar electrodes,[16,17] CuO-derived Cu nanoparticles,[18] CuO-derived three-dimensional (3D) structure,[19] branched CuO/Cu_2O-derived electrodes,[20] and ZnO/Cu_2O for the photocatalytic CO_2RR.[21] Mechanistic studies about the correlation between CO_2RR selectivity and different possible pathways[22] and theoretical work on Cu electrodes,[23] Cu nanoparticles,[24] and facet exposure effect on Cu-based electrocatalysts[25,26] all combined reveal that the product selectivity of CO_2RR in Cu-based materials is a convoluted situation.[27] In addition to the intrinsic catalytic mechanistic factors, a study of CO_2RR on Au opal electrodes demonstrates the effect of mass transport control.[28] Effects of various parameters, such as particle grain size, mass transport, local pH, electrolyte, temperature and pressure, and surface facets, have been summarized in retrospective articles.[5,29]

The nature of the catalyst support can also influence product selectivity. Recent studies suggest that N-doped carbon supports can stabilize Cu in a Cu−N coordination environment during electrolysis and shows the product selectivity toward ethanol or other C2 products.[30−36] Cu on N-doped carbon has also been used in thermal catalysis and shows enhanced stability,[37] and there are reports utilizing N-doped carbon as a catalyst support for electrocatalysis.[38−47] A theoretical study of Cu dimer on C_2N predicts a favored product of C_2H_4.[48] We hypothesize that the N-doped carbon support for CO_2RR will stabilize the intermediate states of CO_2 adsorbates and the catalysts, which leads to specific

Received: August 26, 2022
Accepted: February 2, 2023
Published: February 14, 2023

CO_2RR products, owing to the coordination between the N and the d-orbitals of the metal atoms. In other words, the electron-donating capability of nitrogen atoms can direct the reaction to different pathways.

In this work, we seek to combine the capability of Cu-based catalysts to produce more reduced CO_2RR products and add metal stabilization from the N-doped carbon support. Here, we prepare CuO on graphitic carbon nitride (g-C_3N_4) nanocomposites as the CO_2RR catalysts. Most N-doped carbon supports do not possess evenly and periodically distributed nitrogen dopants. One of the advantages of the selection of g-C_3N_4 as the N-doped carbon support is the even distribution of N and C due to two-dimensional periodicity of g-C_3N_4.[49] Nanocrystals of CuO were prepared, according to reported colloidal synthesis methods with minor modifications,[50,51] in which oleylamine (OAm) and oleic acid (OA) were chosen as the capping agents and reductants,[51] and OAm removal was achieved by thermal treatment of AuNPs at 180 °C overnight.[52]

■ EXPERIMENTAL SECTION

Materials. Copper(II) acetylacetonate (Cu(acac)$_2$, 98%), oleylamine (80−90%), and oleic acid (85−88%) were purchased from Acros Organics. Dicyandiamide (DCDA, 99%) was purchased from Alfa Aesar. Sodium bicarbonate ($NaHCO_3$, 100%) was purchased from Honeywell Fluka. Nafion 117 membrane and 5 wt % Nafion 117 solution (in a mixture of lower aliphatic alcohols and water) were purchased from Giant An Technology. Carbon fiber paper (AvCarb GDS22100) was purchased from HEPHAS Energy. Argon (99.99%), nitrogen (99.99%), carbon dioxide (>99%), and forming gas (5% H_2 and 95% Ar) were purchased from Fung Ming Industrial. Ultrapure water (with a resistivity of 18.2 MΩ·cm) was generated with a Merck Direct-Q3 water purification system. Ferrocenecarboxylic acid (97%) was purchased from Nova Materials. All chemicals were used as received without further purification.

Synthesis of Cupric Oxide (CuO). CuO nanoparticles were synthesized using a modified procedure involving the thermal decomposition of metal acetylacetonate in mixed organic solvents.[27,29,34,53] Typically, 0.5 mmol of Cu(acac)$_2$, 7.5 mL of oleylamine, and 0.16 mL of oleic acid were mixed in a 50 mL single neck round bottom flask equipped with a gas inlet adapter and a Teflon-coated stir bar. Degassing was performed by pumping out the system at room temperature, gradually increasing the temperature to 60 °C, and dwelling for an hour. After degassing, the system was refilled with Ar and heated to 100 °C with a heating ramp of 10 °C/min. After dwelling for 6 h, the reaction was stopped, and the products were isolated and purified with a precipitation and redispersion procedure.

Synthesis of Graphitic Carbon Nitride (g-C_3N_4). Graphitic carbon nitride was prepared by following a two-step synthesis process.[54] Bulk carbon nitride was first synthesized by heating DCDA to 550 °C in air with a heating ramp of 2.3 °C/min and held for 4 h. After grinding, the yellow powder was re-heated to 500 °C in air with a heating ramp of 5 °C/min and a dwelling time of 2 h. The second heat treatment yielded the light yellow graphitic carbon nitride product.

Preparation of g-C_3N_4-Supported CuO. Ten milligrams of CuO was dispersed in 15 mL of hexane. After sonication, 100 mg of g-C_3N_4 was added to the solution, and the mixture was vigorously stirred for 2 h. After settling for 30 min, the clear upper layer and the solid were separated by decanting. The residual solvent in the product composite was removed under vacuum.

Thermal Treatment of g-C_3N_4-Supported CuO. The surface capping agents were removed by heating the composites at 200 °C under reduced pressure for 2 h.[55] After being gradually cooled to room temperature, the system was refilled with forming gas, re-heated to 200 °C, and dwelled for another 2 h to yield the catalyst.[37] Sample labeling and descriptions are summarized in Table S1.

Characterization. Powder X-ray diffraction (PXRD) data were recorded with a Bruker D8 Advance powder X-ray diffractometer with a Cu Kα radiation source (40 kV, 44 mA). Transmission electron microscopy (TEM) images were collected with a JEOL-JEM2100F. TEM samples were prepared by drop-casting on Ni TEM grids. Fourier transform infrared (FTIR) spectra were collected with a Thermo Nicolet 6700. Ultraviolet−visible (UV−vis) spectra were collected with an Agilent Cary 8454. N_2 physisorption measurements were performed with a Micromeritics ASAP 2020. Samples were heated to 120 °C under N_2 flow overnight prior to the physisorption measurements. X-ray photoelectron spectroscopy (XPS) spectra were acquired on a ULVAC PHI 5000 VersaProbe II instrument with a monochromatic Al X-ray source.

Working Electrode Preparation. Carbon fiber paper strips (1 cm × 3 cm) were used as the working electrodes. The catalyst inks were prepared by dispersing 10 mg of CuO or g-C_3N_4-supported CuO (containing 10 mg of CuO) in a solution of 0.5 mL of hexane, 0.5 mL of isopropyl alcohol, and 10 μL of Nafion 117 solution (5% in alcoholic solution). The inks were sonicated for 15 min before drop-casting. In each drop-casting addition, 50 μL of the ink was applied onto the strips in a 1 cm × 1 cm area and dried at 60 °C for 10 min. The drop casting−drying steps were repeated until a total CuO loading of 1 mg/cm^2 was achieved.

Electrochemical Analysis. All electrochemical measurements were conducted with a Bio-Logic SP300 potentiostat/galvanostat with a built-in electrochemical impedance spectroscopy (EIS) analyzer. Reference electrodes ($Ag/AgCl_{(sat.)}$, Aubotech) were externally referenced to a solution of ferrocenecarboxylic acid in 0.2 M phosphate buffer at pH 7 (0.329 V *vs* $Ag/AgCl_{(sat.)}$) prior to each set of experiments, and carbon rods (>99%, Nature World Company) were used as the auxiliary electrodes.

Data were collected using the Bio-Logic EC-Lab software package. All electrochemical measurements were conducted in custom two-compartmented H-cells. The main chamber held the working and reference electrodes in about 100 mL of 0.1 M $NaHCO_3$ solution, while the second chamber held the counter electrode in about 20 mL of 0.1 M $NaHCO_3$ solution. The two compartments were separated with a Nafion 117 membrane. Prior to each set of measurements, the electrolyte solutions were purged with Ar or CO_2 for at least 30 min, and the solution was continuously purged during cyclic voltammetry (CV) measurements. Each electrochemical measurement was repeated at least three times. The uncompensated solution resistance (R_u) was measured with a high-frequency single-point impedance measurement at 100 kHz with a 20 mV amplitude near the open-circuit potential (OCP), and CV and controlled potential electrolysis measurements were corrected for IR drop at 85% through positive feedback using Bio-Logic

https://doi.org/10.1021/acsomega.2c05513
ACS Omega 2023, 8, 7368−7377

EC-Lab software. All electrochemical data were presented *vs* reverse hydrogen electrode (RHE).

For working electrodes that had not been thermally treated, controlled potential experiments at −0.3 V *vs* RHE were performed in separate cells filled with Ar-sparged solutions to preactivate the CuO catalyst by reducing it to Cu.[24,26] Electrochemically active surface area (ECSA) measurements were taken around the open-circuit potential with a 0.1 V window at scan rates ranging from 5 to 200 mV/s.

Product Analysis. Gas-phase products in the headspace after electrolysis were analyzed with a PerkinElmer Clarus 690 gas chromatograph, equipped with an integrated system of custom valves, column configuration, analytical methods, and thermal conductivity detectors (TCDs). The TCDs used Ar as both reference and carrier gas.

Liquid-phase products were analyzed using an Agilent 1260 Infinity II Quaternary Pump system, equipped with an Agilent Hi-Plex H analytical column. Liquid aliquots were taken from the working electrode chamber, and 10 μL of each liquid sample was injected into the sampling loop. The mobile phase was 5 mM H_2SO_4 aqueous solution with a flow rate of 0.6 mL per min. The temperature of the column was maintained at 50 °C. Products were detected using a UV−vis detector (1260 Infinity II variable wavelength detector) and a refractive index detector (1260 Infinity II refractive index detector).

Faradaic Efficiency Calculation. Faradaic efficiency (FE) of each product was calculated with the following equation

$$FE_{(x)} = (n_x \times \text{moles}_x \times F/Q_{\text{total}}) \times 100\%$$

where n_x is the number of electrons involved in each reduction reaction; moles_x is the moles of each product quantified by gas chromatography (GC) or high-performance liquid chromatography (HPLC); F is the Faraday constant, 96,485 C/mol; and Q_{total} is the total charge passed in controlled potential electrolysis experiments (about 50C).

RESULTS AND DISCUSSION

Synthesis and Characterizations of CuO-Derived Nanocomposites. The CuO nanocrystals were synthesized by a modified colloidal synthesis method, which employs the thermal decomposition of copper complexes in a mixture of oleylamine and oleic acid. As shown in Figure 1, the PXRD pattern of the as-synthesized CuO (as-syn CuO) matches well with that of the monoclinic CuO reference (JCPDS Card No. 48-1548) with a grain size of 3.2 nm determined by the Scherrer equation. The representative TEM image of CuO nanocrystals is shown in Figure 2a. Figure S2a shows the particle size distribution acquired from 200 particles, where the average particle size is 2.7 ± 0.2 nm. The selected area electron diffraction (SAED) (Figure 2b) confirms the crystal phase of CuO with the typical ring-like pattern characteristic of nanoparticles. A more detailed TEM image of slightly agglomerated CuO is shown in Figure S1a, and the high-resolution TEM (HRTEM) image (Figure S1b) shows the lattice fringe of CuO(111).

After the first stage of thermal treatment, the PXRD data of thermally treated catalyst under vacuum (labeled as as-syn Cu_2O/Cu) reveals the presence of Cu_2O and Cu. The residual oleylamine molecules enable the partial reduction of CuO to Cu_2O/Cu at elevated temperatures. It has been reported that oleylamine can reduce Cu(II) precursors, and a higher reaction temperature leads to more reduced products.[53] After the consequent heat treatment in forming gas, the PXRD data of the final product (labeled as as-syn Cu) shows the complete transformation to metallic Cu.

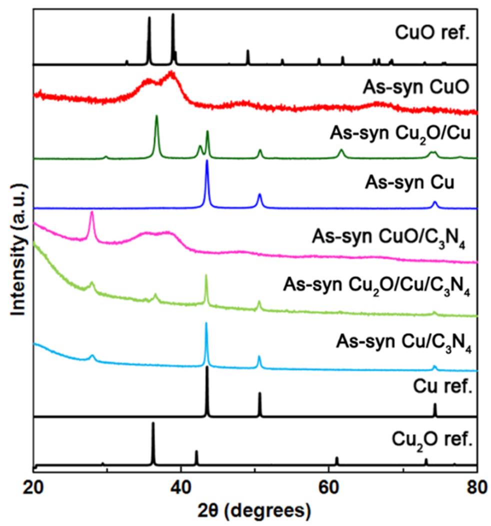

Figure 1. PXRD data of as-syn CuO, as-syn Cu_2O/Cu, as-syn Cu, as-syn CuO/C_3N_4, as-syn Cu_2O/Cu/C_3N_4, as-syn Cu/C_3N_4, and simulated reference patterns JCPDS: Cu (04-0836), Cu_2O (75-1531), and CuO (48-1538).

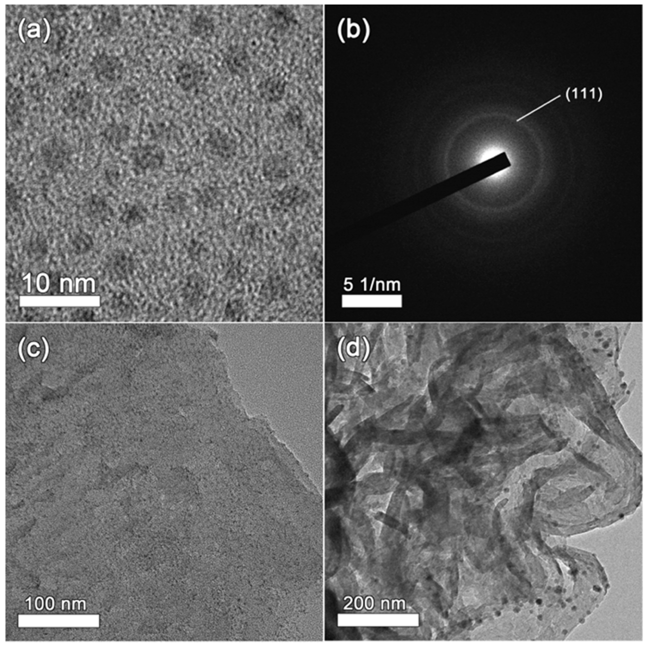

Figure 2. Representative TEM and SAED images of as-syn CuO (a, b) and TEM images of as-syn CuO/C_3N_4 (c) and as-syn Cu/C_3N_4 (d).

The FTIR spectrum of the mixture of oleylamine and oleic acid (Figure 3a) shows the broad N−H stretching vibration at around 3400 cm^{-1}, asymmetric C−H stretching vibrations at 2918 and 2850 cm^{-1}, C=C bending vibration at 1650 cm^{-1}, C−H stretching vibration at 1550 cm^{-1}, C−H bending vibrations at 1458 and 1400 cm^{-1}, and C−C bending vibration at 700 cm^{-1}. The FTIR spectrum of as-syn CuO (Figure 3b) shows the presence of the aforementioned peaks. The FTIR spectrum of as-syn Cu_2O/Cu (Figure 3c) reveals that no significant characteristic peaks of oleylamine or oleic acid are

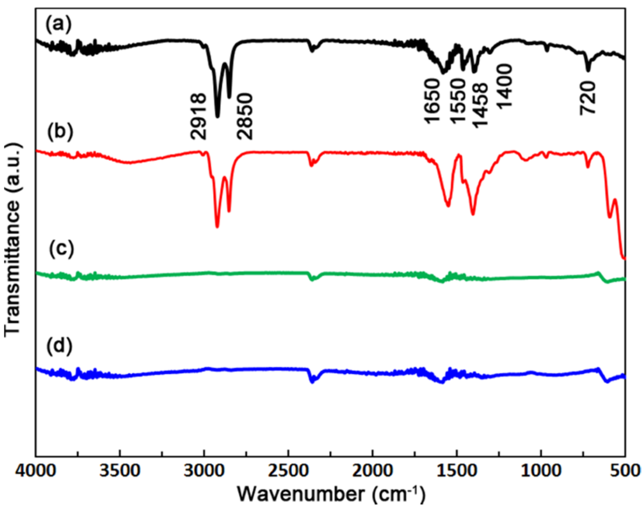

Figure 3. FTIR spectra of a mixture of oleylamine and oleic acid (a), as-syn CuO (b), as-syn CuO/Cu (c), and as-syn Cu (d).

detectable, and it confirms the successful removal of the ligands by thermal treatment under vacuum. The FTIR spectrum of as-syn Cu (Figure 3d) reveals the absence of those of oleylamine or oleic acid as well.

Figure S3 shows the thermogravimetric analysis (TGA) thermogram of as-syn CuO. The first weight loss before 200 °C, *ca.* 9%, could be attributed to the removal of physisorbed water, and the weight loss between 200 to 350 °C, *ca.* 51%, could be assigned to the removal of organic content, *i.e.*, oleylamine and oleic acid. Thermal treatment at this temperature in vacuum facilitates the evaporation of the capping agents.

We attempted to remove ligands by acid treatment (data not shown), as achieved in other colloidal syntheses with oleylamine ligands.[55,56] However, the acidic environment induced problems of instability and corrosion of CuO, which resulted in blue-colored solutions.

Synthesis and Characterizations of *g*-C_3N_4 Support. The *g*-C_3N_4 nanosheets were prepared by a two-step synthesis method.[54] In Figure S4, the PXRD diffraction patterns consist of reflections from the graphite structure and tri-s-triazine units, which have been documented in previous reports.[49,57−59] The major peak at *ca.* 27° is indexed as (002), representing the interlayer separation of the graphitic material, and the broad peak at *ca.* 13° represents the in-plane packing of motif (100), which is equivalent to a *d*-spacing of 0.7 nm. The slight shift of the (002) peak of the *g*-C_3N_4 nanosheets toward a wider angle compared to the bulk *g*-C_3N_4 is possibly due to the reduced interplanar separation after the second thermal treatment.

The specific surface area of bulk *g*-C_3N_4 and *g*-C_3N_4 nanosheets was measured by nitrogen physisorption. The calculation based on the multipoint Brunauer−Emmett−Teller (BET) (Figure S5) shows the increase of specific surface area after the second thermal treatment, *i.e.*, the increase from 19.79 ± 0.06 to 91.84 ± 0.53 m^2/g.

Preparation of *g*-C_3N_4-Supported Nanocomposites. The *g*-C_3N_4-supported CuO nanocomposites were prepared by adding controlled amounts of *g*-C_3N_4 nanosheets to a suspension of CuO in hexane, followed by vigorous mixing, decanting, and drying in vacuum. Figure 2c shows the TEM of as-synthesized *g*-C_3N_4-supported CuO (as-syn CuO/C_3N_4). The CuO nanocrystals are well separated on the *g*-C_3N_4 support with a nominal loading of 9 wt %. The residual oleylamine and oleic acid might serve as a protective layer to prevent potential aggregation during the drying process, while the van der Waals force between the small CuO particles and *g*-C_3N_4 also contributes to maintain particle separation. The PXRD patterns of supported CuO nanocomposites at different stages of thermal treatment are shown in Figure 1. Similar to the unsupported CuO, thermal treatment of as-syn CuO/C_3N_4 first yields a mixture of Cu_2O and Cu. XRD peaks of Cu_2O

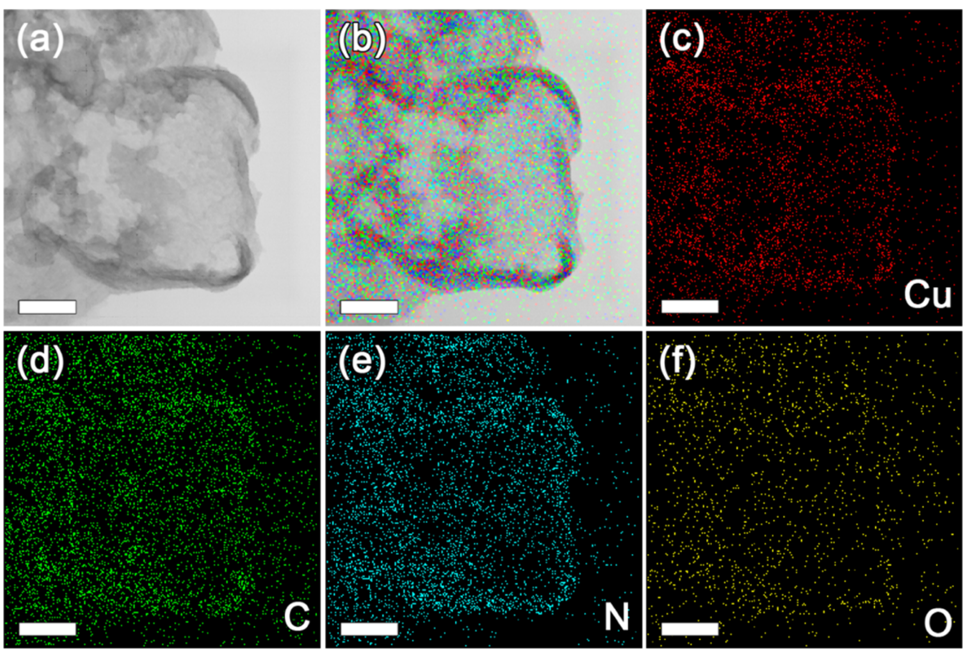

Figure 4. TEM of as-syn CuO/C_3N_4 (a), superimposed TEM and EDS elemental mapping (b), and individual EDS elemental mapping images of Cu, C, N, and O (c−f); scale bar of 200 nm.

https://doi.org/10.1021/acsomega.2c05513
ACS Omega 2023, 8, 7368−7377

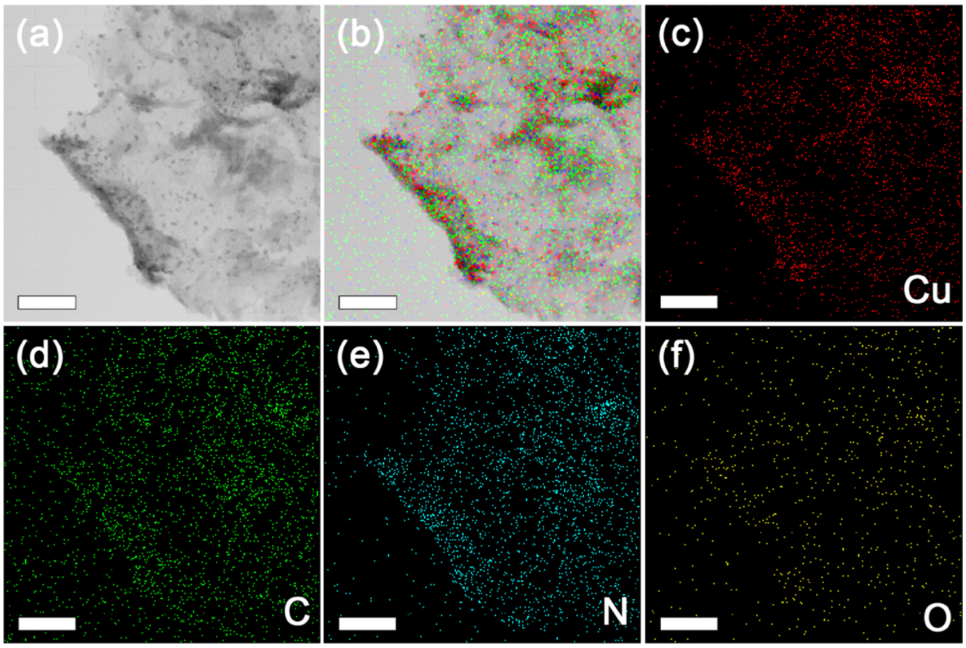

Figure 5. TEM of as-syn Cu/C_3N_4 (a), superimposed TEM and EDS elemental mapping (b), and individual EDS elemental mapping images of Cu, C, N, and O (c–f); scale bar of 200 nm.

were present in as-syn $Cu_2O/Cu/C_3N_4$ but were not as intense as in the unsupported as-syn CuO. This might be due to the presence of more residual oleylamine, which has some reductive capability, on the *g*-C_3N_4 support. Additional thermal treatment with forming gas completes the conversion to Cu nanoparticles on *g*-C_3N_4 nanosheets (as-syn Cu/C_3N_4).

Energy-dispersive spectroscopy (EDS) elemental mapping was performed to investigate the CuO particle dispersion on *g*-C_3N_4 nanosheets. In Figure 4, the individual elemental mapping images and the superimposed image all reveal an even distribution of the CuO particles without noticeable agglomeration or phase segregation. Figure 2d shows the TEM of as-syn Cu/C_3N_4 after two-stage thermal treatment. After the removal of capping agents and thermal reduction in forming gas, more distinct particles appear near the edges of the folded structure with an average particle size of 6.0 ± 0.7 nm. The particle size distribution is shown in Figure S2b. The EDS mapping images, Figure 5c–e, of C, N, and Cu show no significant difference while the O signal intensity, Figure 5f, decreases slightly compared to that of the as-syn CuO/C_3N_4. The slightly weaker O signal intensity could be due to the formation of surface oxide, which is inevitable after the system is re-exposed to air.

Prereduction of Nonthermally Treated Samples. CV of as-syn CuO, Figure 6, shows two reduction peaks at around 0.4 and −0.1 V *vs* RHE, which are attributed to the Cu(II)/Cu(I) and Cu(I)/Cu(0) reduction couples, respectively,[60] although the theoretical reduction potentials of both steps are slightly more positive.[5] The convoluted oxidation peak might be due to a mix of Cu(0)/Cu(I) and Cu(I)/Cu(II) oxidation processes. To ensure that the catalysts were completely reduced to Cu, controlled potential pretreatments at −0.3 V *vs* RHE were performed. Chronoamperometry data, Figure S6, shows that the reduction completes within 10 minutes. The absence of the distinct oxidation−reduction features in the CVs of *g*-C_3N_4-supported composites might be due to the capacitance of the *g*-C_3N_4 matrix masking the peaks.

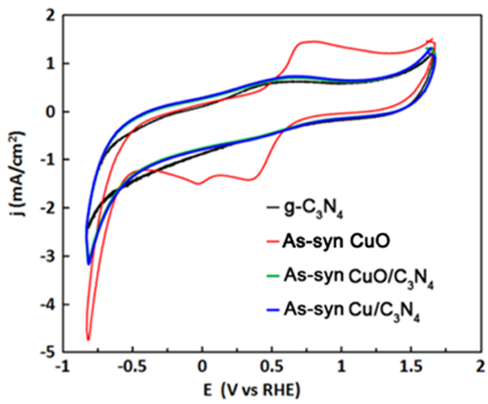

Figure 6. CVs of *g*-C_3N_4 (black), as-syn CuO (red), as-syn CuO/C_3N_4 (green), and as-syn Cu/C_3N_4 (blue) in Ar-sparged 0.1 M $NaHCO_3$ solutions.

Effectiveness of Removal of Capping Agents. Figure S7a–c shows the CVs of the *g*-C_3N_4 nanosheets, as-syn CuO/C_3N_4, and as-syn Cu/C_3N_4. Figure S7d reveals the linear plot of capacitive currents of the non-Faradaic region, at 0.95 V *vs* RHE, with different scan rates of 5, 10, 25, 50, 100, 150, and 200 mV/s, and the slope of the plot leads to the estimated double-layer capacitance (C_{dl}) of each electrode. The C_{dl} serves as a quantitative evaluation of the electrochemically active surface areas because the direct measurement of surface active sites is not available. The C_{dl} of as-syn CuO/*g*-C_3N_4 is only slightly higher than those of *g*-C_3N_4 nanosheets. This could be attributed to the relatively small accessible surface area of ligand-capped CuO compared to the *g*-C_3N_4 nanosheets, which possess a specific surface area of 91.84 ± 0.53 m^2/g. After thermal treatment, the C_{dl} increases by *ca.* 42%, suggesting that more surface active sites are available. Nevertheless, the particle size estimation based on PXRD and TEM reveals the particle growth after thermal treatment.

https://doi.org/10.1021/acsomega.2c05513
ACS Omega 2023, 8, 7368−7377

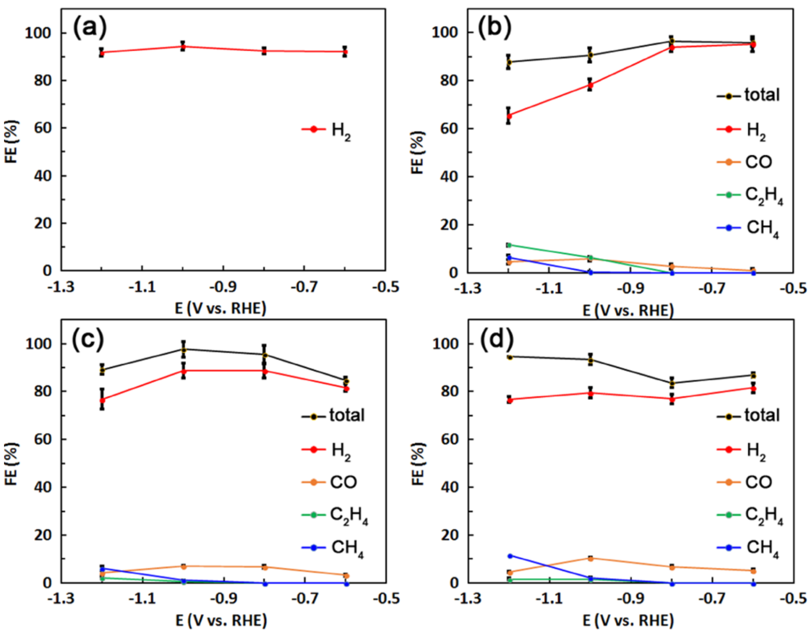

Figure 7. Electrochemical CO_2RR activities presented in terms of FEs of $H_2/CO/C_2H_4/CH_4$: (a) *g*-C_3N_4, (b) as-syn CuO, (c) as-syn CuO/C_3N_4, and (d) as-syn Cu/C_3N_4.

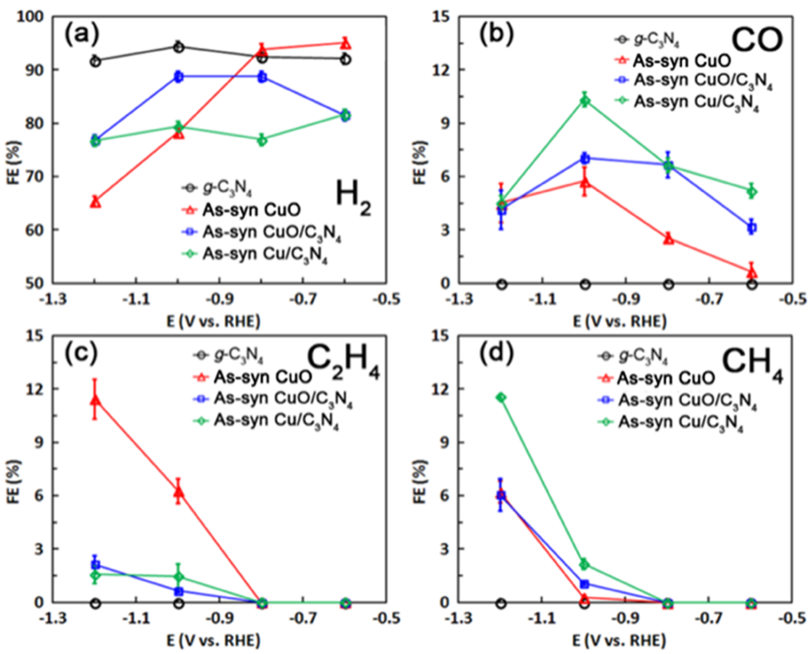

Figure 8. Electrochemical CO_2RR activity comparisons by products: (a) H_2, (b) CO, (c) C_2H_4, and (d) CH_4.

Electrochemical CO_2RR Activity Measurements. CVs of carbon paper, *g*-C_3N_4 nanosheets, unsupported CuO, as-syn CuO/*g*-C_3N_4, and as-syn Cu/*g*-C_3N_4 are shown in Figure S8. The carbon paper and *g*-C_3N_4 nanosheets show no CO_2RR activity, while the *g*-C_3N_4 support shows a larger current response at more negative potential. An earlier study suggests that low CO_2RR activity is observed when only *g*-C_3N_4 nanosheets are present.[61] CuO, as-syn CuO/C_3N_4, and as-syn Cu/C_3N_4 demonstrate CO_2RR capability. Among the *g*-C_3N_4 supported catalysts, the as-syn Cu/C_3N_4 shows nearly double current response compared to as-syn CuO/C_3N_4. This increase could be attributed to the increase in surface active sites after capping agent removal, in agreement with the ECSA measurements.

Aside from specific activity, product selectivity is another measurement for evaluating catalyst performance. Figure 7 shows the CO_2RR product distributions of controlled potential electrolysis experiments of different samples at −0.6, −0.8, −1.0, and −1.2 V *vs* RHE. The *g*-C_3N_4 support only produces H_2 while others produce different amounts of $H_2/CO/C_2H_4/CH_4$. More reduced products are observed at more negative potentials, which is consistent with findings of electrochemical CO_2RR by Cu-based catalysts in previous studies.[62,63] Figure 8 shows the comparison of Faradaic efficiency (FE) in different samples. The CuO, as-syn CuO/C_3N_4, and as-syn Cu/C_3N_4

show the FE of H_2 ranging from 70−80% and the FEs of CO/CH_4/C_2H_4 near 10%. For the production of CO, *g*-C_3N_4-supported catalysts show slightly more positive onset potential than CuO. The unsupported CuO shows the highest production of C_2H_4, while as-syn Cu/C_3N_4 has the highest production of CH_4.

Several factors might contribute to the discrepancy between the electrochemical CO_2RR performance of samples with or without *g*-C_3N_4 support. Carbon paper support has a specific surface area of about several m^2 per gram, and the equivalent real surface area per 1 cm^2 of geometric surface area of working electrodes is about 50 cm^2.[64] The 10 mg of *g*-C_3N_4 loadings has a total surface area of 9000 cm^2, which is two orders of magnitude greater than the carbon paper support. In other words, the catalyst dispersion density on carbon paper is two orders of magnitude greater than that on *g*-C_3N_4/carbon paper.

This huge difference in dispersion density leads to different spatial separation of CuO particles. For the sample of CuO on carbon paper, the electrochemical prereduction causes particle aggregation, *i.e.*, particle size growth. Surface reconstruction of Cu during electrolysis induces particle growth as well.[65] Several recent reports also demonstrate similar effects on supported/unsupported Cu_2O-derived catalysts and their effects on electrochemical CO_2RR product selectivity.[62,66,67] In an earlier report of Cu catalysts on a Si wafer, the authors attribute the difference between electrochemical CO_2RR product selectivity of particles with various sizes to the number of atoms possessing under-coordinated facets.[63] Computational studies suggest that product selectivity depends on the interaction between the intermediates and various facets.[48,68−72] The growth of crystals leads to different facet populations, which affect the surface affinities toward different adsorbates/intermediates.

In addition to different facet populations, catalyst dispersion also affects the local mass transport of reactants/intermediates. In the case of high catalyst dispersion density, the less spatially separated active sites increase the probability of the readsorption of the intermediates, and the limited mass transport causes local depletion of proton supply. As a result, the C2 product is favored over C1 products when *g*-C_3N_4 is absent, and vice versa. A recent computational study suggests that Cu species can be stabilized in a C_2N porous matrix due to the hybridization of Cu 3d orbitals and N 2p orbitals. This makes CH_4 the favored electrochemical CO_2RR product,[48] which is consistent with our results from *g*-C_3N_4-supported specimens.

***Ex Situ* XPS Measurement of Selected Samples at Different Stages.** XPS data of as-syn CuO/C_3N_4, as-syn Cu/C_3N_4, and post-CO_2RR Cu/C_3N_4 were collected to serve as the complementary evidence to the oxidation states and chemical environments of Cu and C in the specimens. The C spectra (Figure S9) show a decrease of the relative peak intensity at *ca.* 284 eV (C−C) in as-syn Cu/C_3N_4 compared to as-syn CuO/C_3N_4. This confirms the successful removal of alkyl ligands, which is also observed by the FTIR measurement. The additional peak at *ca.* 291 eV (C═O) in post-CO_2RR Cu/C_3N_4 reveals the residual carbonates from the electrolytes $[CO_3]^{2-}$ and $[HCO_3]^-$.

The Cu spectra (Figure S10) show the transition from Cu(II) in CuO/C_3N_4 to Cu(0) in Cu/C_3N_4. In the XPS of CuO/C_3N_4, the satellite peaks at *ca.* 960 and 950 eV are characteristic peaks of Cu(II) species. These peaks are absent in the spectra of as-syn Cu/C_3N_4 and post-CO_2RR Cu/C_3N_4, suggesting a reduced form of Cu. There is no noticeable difference in Cu XPS before and after electrolysis, implying no significant oxidation state change.

CONCLUSIONS

We have successfully prepared CuO-derived catalysts for the electrochemical CO_2RR. A two-stage thermal treatment leads to the successful removal of the capping agents and reduction to Cu. An organic moiety removal is verified by FTIR and XPS measurements, and CV measurements also confirm the increase of electrochemically active surface area after thermal treatment.

For the electrochemical CO_2RR product selectivity of more reduced products, CuO shows the highest selectivity toward C_2H_4, while the *g*-C_3N_4-supported CuO catalysts yield more CH_4. We attribute this selectivity discrepancy to three major possible factors: (1) the change of the surface dominant facets due to particle growth, (2) the ensemble effect induced by different catalyst loading densities, and (3) the hybridization and stabilization of the catalyst−support interaction. By precise control of the experimental parameters, we believe that this will enable the design and fabrication of catalyst systems with narrower product distribution of hydrocarbons over H_2 or CO.

ASSOCIATED CONTENT

Supporting Information

The Supporting Information is available free of charge at https://pubs.acs.org/doi/10.1021/acsomega.2c05513.

g-C_3N_4 characterizations, TEMs, CVs, XPS, and ECSA measurements (PDF)

AUTHOR INFORMATION

Corresponding Authors

Yu-Hsu Chang − *Institute of Mineral Resources Engineering, Department of Materials and Mineral Resources Engineering, National Taipei University of Technology, Taipei 106344, Taiwan;* orcid.org/0000-0003-2813-6383; Email: yhchang@ntut.edu.tw

Chia-Cheng Lin − *Institute of Mineral Resources Engineering, Department of Materials and Mineral Resources Engineering, National Taipei University of Technology, Taipei 106344, Taiwan;* orcid.org/0000-0002-7550-1577; Email: johncclin@ntut.edu.tw

Authors

Chien-Lin Sung − *Institute of Mineral Resources Engineering, Department of Materials and Mineral Resources Engineering, National Taipei University of Technology, Taipei 106344, Taiwan*

Ren-Hung Wang − *Institute of Mineral Resources Engineering, Department of Materials and Mineral Resources Engineering, National Taipei University of Technology, Taipei 106344, Taiwan*

You-Cheng Shih − *Institute of Mineral Resources Engineering, Department of Materials and Mineral Resources Engineering, National Taipei University of Technology, Taipei 106344, Taiwan;* orcid.org/0000-0002-0096-7997

Zhi-Ying Wu − *Institute of Mineral Resources Engineering, Department of Materials and Mineral Resources Engineering, National Taipei University of Technology, Taipei 106344, Taiwan*

https://doi.org/10.1021/acsomega.2c05513
ACS Omega 2023, 8, 7368−7377

Samuel R. Alvarado − *Department of Chemistry and Biotechnology, University of Wisconsin−River Falls, River Falls, Wisconsin 54022, United States*

Complete contact information is available at:
https://pubs.acs.org/10.1021/acsomega.2c05513

Author Contributions

§C.-L.S. and R.-H.W. contributed equally to this work.

Notes

The authors declare no competing financial interest.

■ ACKNOWLEDGMENTS

This work was supported by the Ministry of Science and Technology in Taiwan (MOST 109-2113-M-027-001-MY3) and (MOST 110-2113-M-027-008).

■ REFERENCES

(1) Kakran, S.; Chanana, S. Smart operations of smart grids integrated with distributed generation: A review. *Renewable Sustainable Energy Rev.* **2018**, *81*, 524−535.
(2) González, A.; Goikolea, E.; Barrena, J. A.; Mysyk, R. Review on supercapacitors: Technologies and materials. *Renewable Sustainable Energy Rev.* **2016**, *58*, 1189−1206.
(3) De Luna, P.; Hahn, C.; Higgins, D.; Jaffer, S. A.; Jaramillo, T. F.; Sargent, E. H. What would it take for renewably powered electrosynthesis to displace petrochemical processes? *Science* **2019**, *364*, No. eaav3506.
(4) Li, W. Electrocatalytic Reduction of CO_2 to Small Organic Molecule Fuels on Metal Catalysts. In *Advances in CO_2 Conversion and Utilization*; Hu, Y. H., Ed.; American Chemical Society: Washington, DC, USA, 2010; pp 55−76.
(5) Nitopi, S.; Bertheussen, E.; Scott, S. B.; Liu, X.; Engstfeld, A. K.; Horch, S.; Seger, B.; Stephens, I. E. L.; Chan, K.; Hahn, C.; Nørskov, J. K.; Jaramillo, T. F.; Chorkendorff, I. Progress and Perspectives of Electrochemical CO2 Reduction on Copper in Aqueous Electrolyte. *Chem. Rev.* **2019**, *119*, 7610−7672.
(6) Kuhl, K. P.; Hatsukade, T.; Cave, E. R.; Abram, D. N.; Kibsgaard, J.; Jaramillo, T. F. Electrocatalytic Conversion of Carbon Dioxide to Methane and Methanol on Transition Metal Surfaces. *J. Am. Chem. Soc.* **2014**, *136*, 14107−14113.
(7) Kuhl, K. P.; Cave, E. R.; Abram, D. N.; Jaramillo, T. F. New insights into the electrochemical reduction of carbon dioxide on metallic copper surfaces. *Energy Environ. Sci.* **2012**, *5*, 7050−7059.
(8) Terunuma, Y.; Saitoh, A.; Momose, Y. Relationship between hydrocarbon production in the electrochemical reduction of CO_2 and the characteristics of the Cu electrode. *J. Electroanal. Chem.* **1997**, *434*, 69−75.
(9) Hori, Y.; Murata, A.; Takahashi, R. Formation of Hydrocarbons in the Electrochemical Reduction of Carbon Dioxide at a Copper Electrode in Aqueous Solution. *J. Chem. Soc., Faraday Trans. 1* **1989**, *85*, 2309−2326.
(10) Sen, S.; Liu, D.; Palmore, G. T. R. Electrochemical Reduction of CO2 at Copper Nanofoams. *ACS Catal.* **2014**, *4*, 3091−3095.
(11) Le, M.; Ren, M.; Zhang, Z.; Sprunger, P. T.; Kurtz, R. L.; Flake, J. C. Electrochemical Reduction of CO_2 to CH_3OH at Copper Oxide Surfaces. *J. Electrochem. Soc.* **2011**, *158*, E45−E49.
(12) Ke, F.-S.; Liu, X.-C.; Wu, J.; Sharma, P. P.; Zhou, Z.-Y.; Qiao, J.; Zhou, X.-D. Selective formation of C2 products from the electrochemical conversion of CO_2 on CuO-derived copper electrodes comprised of nanoporous ribbon arrays. *Catal. Today* **2017**, *288*, 18−23.
(13) Li, D.; Huang, L.; Liu, T.; Liu, J.; Zhen, L.; Wu, J.; Feng, Y. Electrochemical reduction of carbon dioxide to formate via nanoprism assembled CuO microspheres. *Chemosphere* **2019**, *237*, No. 124527.
(14) Ma, M.; Djanashvili, K.; Smith, W. A. Selective Electrochemical Reduction of CO_2 to CO on CuO-Derived Cu Nanowires. *Phys. Chem. Chem. Phys.* **2015**, *17*, 20861−20867.
(15) Mistry, H.; Varela, A. S.; Bonifacio, C. S.; Zegkinoglou, I.; Sinev, I.; Choi, Y. W.; Kisslinger, K.; Stach, E. A.; Yang, J. C.; Strasser, P.; Cuenya, B. R. Highly Selective Plasma-Activated Copper Catalysts for Carbon Dioxide Reduction to Ethylene. *Nat. Commun.* **2016**, *7*, No. 12123.
(16) Li, C. W.; Ciston, J.; Kanan, M. W. Electroreduction of carbon monoxide to liquid fuel on oxide-derived nanocrystalline copper. *Nature* **2014**, *508*, 504−507.
(17) Verdaguer-Casadevall, A.; Li, C. W.; Johansson, T. P.; Scott, S. B.; McKeown, J. T.; Kumar, M.; Stephens, I. E. L.; Kanan, M. W.; Chorkendorff, I. Probing the Active Surface Sites for CO Reduction on Oxide-Derived Copper Electrocatalysts. *J. Am. Chem. Soc.* **2015**, *137*, 9808−9811.
(18) Feng, X.; Jiang, K.; Fan, S.; Kanan, M. W. A Direct Grain-Boundary-Activity Correlation for CO Electroreduction on Cu Nanoparticles. *ACS Cent. Sci.* **2016**, *2*, 169−174.
(19) Raciti, D.; Wang, Y.; Park, J. H.; Wang, C. Three-Dimensional Hierarchical Copper-Based Nanostructures as Advanced Electrocatalysts for CO_2 Reduction. *ACS Appl. Energy Mater.* **2018**, *1*, 2392−2398.
(20) Kim, J.; Choi, W.; Park, J. W.; Kim, C.; Kim, M.; Song, H. Branched Copper Oxide Nanoparticles Induce Highly Selective Ethylene Production by Electrochemical Carbon Dioxide Reduction. *J. Am. Chem. Soc.* **2019**, *141*, 6986−6994.
(21) Bae, K.-L.; Kim, J.; Lim, C. K.; Nam, K. M.; Song, H. Colloidal zinc oxide-copper(I) oxide nanocatalysts for selective aqueous photocatalytic carbon dioxide conversion into methane. *Nat. Commun.* **2017**, *8*, No. 1156.
(22) Schouten, K. J. P.; Kwon, Y.; van der Ham, C. J. M.; Qin, Z.; Koper, M. T. M. A new mechanism for the selectivity to C1 and C2 species in the electrochemical reduction of carbon dioxide on copper electrodes. *Chem. Sci.* **2011**, *2*, 1902−1909.
(23) Nie, X.; Esopi, M. R.; Janik, M. J.; Asthagiri, A. Selectivity of CO_2 Reduction on Copper Electrodes: The Role of the Kinetics of Elementary Steps. *Angew. Chem., Int. Ed.* **2013**, *52*, 2459−2462.
(24) Dong, H.; Li, Y.; Jiang, D.-E. First-Principles Insight into Electrocatalytic Reduction of CO_2 to CH_4 on a Copper Nanoparticle. *J. Phys. Chem. C* **2018**, *122*, 11392−11398.
(25) Keerthiga, G.; Viswanathan, B.; Chetty, R. Electrochemical reduction of CO_2 on electrodeposited Cu electrodes crystalline phase sensitivity on selectivity. *Catal. Today* **2015**, *245*, 68−73.
(26) Luo, W.; Nie, X.; Janik, M. J.; Asthagiri, A. Facet Dependence of CO_2 Reduction Paths on Cu Electrodes. *ACS Catal.* **2016**, *6*, 219−229.
(27) Bagger, A.; Ju, W.; Varela, A. S.; Strasser, P.; Rossmeisl, J. Electrochemical CO_2 Reduction: A Classification Problem. *ChemPhysChem* **2017**, *18*, 3266−3273.
(28) Hall, A. S.; Yoon, Y.; Wuttig, A.; Surendranath, Y. Mesostructure-Induced Selectivity in CO_2 Reduction Catalysis. *J. Am. Chem. Soc.* **2015**, *137*, 14834−14837.
(29) Raciti, D.; Wang, C. Recent Advances in CO_2 Reduction Electrocatalysis on Copper. *ACS Energy Lett.* **2018**, *3*, 1545−1556.
(30) Karapinar, D.; Huan, N. T.; Sahraie, N. R.; Li, J.; Wakerley, D.; Touati, N.; Zanna, S.; Taverna, D.; Tizei, L. H. G.; Zitolo, A.; Jaouen, F.; Mougel, V.; Fontecave, M. Electroreduction of CO_2 on Single-Site Copper-Nitrogen-Doped Carbon Material: Selective Formation of Ethanol and Reversible Restructuration of the Metal Sites. *Angew. Chem., Int. Ed.* **2019**, *58*, 15098−15103.
(31) Zhao, K.; Liu, Y.; Quan, X.; Chen, S.; Yu, H. CO_2 Electroreduction at Low Overpotential on Oxide-Derived Cu/Carbons Fabricated from Metal Organic Framework. *ACS Appl. Mater. Interfaces* **2017**, *9*, 5302−5311.
(32) Chen, C.; Yan, X.; Liu, S.; Wu, Y.; Wan, Q.; Sun, X.; Zhu, Q.; Liu, H.; Ma, J.; Zheng, L.; Wu, H.; Han, B. Highly Efficient Electroreduction of CO_2 to C2+ Alcohols on Heterogeneous Dual Active Sites. *Angew. Chem., Int. Ed.* **2020**, *59*, 16459−16464.

(33) Wang, H.; Tzeng, Y.-K.; Ji, Y.; Li, Y.; Li, J.; Zheng, X.; Yang, A.; Liu, Y.; Gong, Y.; Cai, L.; Li, Y.; Zhang, X.; Chen, W.; Liu, B.; Lu, H.; Melosh, N. A.; Shen, Z.-X.; Chan, K.; Tan, T.; Chu, S.; Cui, Y. Synergistic enhancement of electrocatalytic CO_2 reduction to C_2 oxygenates at nitrogen-doped nanodiamonds/Cu interface. *Nat. Nanotechnol.* **2020**, *15*, 131−137.
(34) Zarandi, R. F.; Rezaei, B.; Ghaziaskar, H. S.; Ensafi, A. A. Modification of Copper Electrode with Copper Nanoparticles@ Reduced Graphene Oxide-Nile Blue and Its Application in Electrochemical CO_2 Conversion. *Mater. Today Energy* **2020**, *18*, No. 100507.
(35) Li, Q.; Zhu, W.; Fu, J.; Zhang, H.; Wu, G.; Sun, S. Controlled assembly of Cu nanoparticles on pyridinic-N rich graphene for electrochemical reduction of CO2 to ethylene. *Nano Energy* **2016**, *24*, 1−9.
(36) Wang, X.; Wang, Z.; de Arquer, F. P. G.; Dinh, C.-T.; Ozden, A.; Li, Y. C.; Nam, D.-H.; Li, J.; Liu, Y.-S.; Wicks, J.; Chen, Z.; Chi, M.; Chen, B.; Wang, Y.; Tam, J.; Howe, J. Y.; Proppe, A.; Todorović, P.; Li, F.; Zhuang, T.-T.; Gabardo, C. M.; Kirmani, A. R.; McCallum, C.; Hung, S.-F.; Lum, Y.; Luo, M.; Min, Y.; Xu, A.; O'Brien, C. P.; Stephen, B.; Sun, B.; Ip, A. H.; Richter, L. J.; Kelley, S. O.; Sinton, D.; Sargent, E. H. Efficient electrically powered CO_2-to-ethanol via suppression of deoxygenation. *Nat. Energy* **2020**, *5*, 478−486.
(37) Bulushev, D. A.; Chuvilin, A. L.; Sobolev, V. I.; Stolyarova, S. G.; Shubin, Y. V.; Asanov, I. P.; Ishchenko, A. V.; Magnani, G.; Riccò, M.; Okotrub, A. V.; Bulusheva, L. G. Copper on carbon materials: stabilization by nitrogen doping. *J. Mater. Chem. A* **2017**, *5*, 10574−10583.
(38) Liu, Z.; Cao, J.; Wu, B.; Qian, L.; Guan, A.; Yang, C.; Lv, X.; Zhang, L.; Zheng, G. Surface Energy Tuning on Cu/NC Catalysts for CO Electroreduction. *ACS Catal.* **2022**, *12*, 12555−12562.
(39) Zhang, J.; Guo, Y.; Shang, B.; Fan, T.; Lian, X.; Huang, P.; Dong, Y.; Chen, Z.; Yi, X. Unveiling the Synergistic Effect between Graphitic Carbon Nitride and Cu_2O toward CO_2 Electroreduction to C_2H_4. *ChemSusChem* **2021**, *14*, 929−937.
(40) Li, H.; Cao, S.; Sun, H.; Lu, Y.; Zhang, Y.; Lu, X.; Zeng, J.; Yan, Z. CuNCN derived Cu-based/CxNy catalysts for highly selective CO_2 electroreduction to hydrocarbons. *Appl. Catal., B* **2023**, *320*, No. 121948.
(41) Pan, Y.; Li, H.; Xiong, J.; Yu, Y.; Du, H.; Li, S.; Wu, Z.; Li, S.; Lai, J.; Wang, L. Protecting the state of Cu clusters and nanoconfinement engineering over hollow mesoporous carbon spheres for electrocatalytical C-C coupling. *Appl. Catal., B* **2022**, *306*, No. 121111.
(42) Zhao, S.; Tang, Z.; Guo, S.; Han, M.; Zhu, C.; Zhou, Y.; Bai, L.; Gao, J.; Huang, H.; Li, Y.; Liu, Y.; Kang, Z. Enhanced Activity for CO_2 Electroreduction on a Highly Active and Stable Ternary Au-CDots-C_3N_4 Electrocatalyst. *ACS Catal.* **2018**, *8*, 188−197.
(43) Woyessa, G. W.; dela Cruz, J.-a. B.; Rameez, M.; Hung, C.-H. Nanocomposite catalyst of graphitic carbon nitride and Cu/Fe mixed metal oxide for electrochemical CO2 reduction to CO. *Appl. Catal., B* **2021**, *291*, No. 120052.
(44) Zhang, L.; Mao, F.; Zheng, L. R.; Wang, H. F.; Yang, X. H.; Yang, H. G. Tuning Metal Catalyst with Metal−C_3N_4 Interaction for Efficient CO_2 Electroreduction. *ACS Catal.* **2018**, *8*, 11035−11041.
(45) Jiao, Y.; Zheng, Y.; Chen, P.; Jaroniec, M.; Qiao, S.-Z. Molecular Scaffolding Strategy with Synergistic Active Centers To Facilitate Electrocatalytic CO_2 Reduction to Hydrocarbon/Alcohol. *J. Am. Chem. Soc.* **2017**, *139*, 18093−18100.
(46) Fu, S.; Liu, X.; Ran, J.; Jiao, Y.; Qiao, S.-Z. CO_2 reduction by single copper atom supported on g-C_3N_4 with asymmetrical active sites. *Appl. Surf. Sci.* **2021**, *540*, No. 148293.
(47) Lin, W.; Chen, H.; Li, Z.; Sasaki, K.; Yao, S.; Zhang, Z.; Li, J.; Fu, J. A Cu_2O-derived Polymeric Carbon Nitride Heterostructured Catalyst for the Electrochemical Reduction of Carbon Dioxide to Ethylene. *ChemSusChem* **2021**, *14*, 3190−3197.
(48) Zhao, J.; Zhao, J.; Li, F.; Chen, Z. Copper Dimer Supported on A C_2N Layer as an Efficient Electrocatalyst for Co_2 Reduction Reaction: A Computational Study. *J. Phys. Chem. C* **2018**, *122*, 19712−19721.
(49) Thomas, A.; Fischer, A.; Goettmann, F.; Antonietti, M.; Müller, J.-O.; Schlögl, R.; Carlsson, J. M. Graphitic Carbon Nitride Materials: Variation of Structure and Morphology and Their Use as Metal-Free Catalysts. *J. Mater. Chem.* **2008**, *18*, 4893−4908.
(50) Mourdikoudis, S.; Liz-Marzán, L. M. Oleylamine in Nanoparticle Synthesis. *Chem. Mater.* **2013**, *25*, 1465−1476.
(51) Zhang, J.; Fang, J. A General Strategy for Preparation of Pt 3d-Transition Metal (Co, Fe, Ni) Nanocubes. *J. Am. Chem. Soc.* **2009**, *131*, 18543−18547.
(52) Zhu, W.; Michalsky, R.; Metin, Ö.; Lv, H.; Guo, S.; Wright, C. J.; Sun, X.; Peterson, A. A.; Sun, S. Monodisperse Au Nanoparticles for Selective Electrocatalytic Reduction of CO_2 to CO. *J. Am. Chem. Soc.* **2013**, *135*, 16833−16836.
(53) Liu, X. W.; Geng, B. Y.; Du, Q. B.; Ma, J. Z.; Liu, X. M. Temperature-Controlled Self-Assembled Synthesis of CuO,Cu_2O and Cu Nanoparticles through a Single-Precursor Route. *Mater. Sci. Eng.: A* **2007**, *448*, 7−14.
(54) Niu, P.; Zhang, L.; Liu, G.; Cheng, H. M. Graphene-Like Carbon Nitride Nanosheets for Improved Photocatalytic Activities. *Adv. Funct. Mater.* **2012**, *22*, 4763−4770.
(55) Li, D.; Wang, C.; Tripkovic, D.; Sun, S.; Markovic, N. M.; Stamenkovic, V. R. Surfactant Removal for Colloidal Nanoparticles from Solution Synthesis: The Effect on Catalytic Performance. *ACS Catal.* **2012**, *2*, 1358−1362.
(56) Lee, Y. H.; Lee, G.; Shim, J. H.; Hwang, S.; Kwak, J.; Lee, K.; Song, H.; Park, J. T. Monodisperse PtRu Nanoalloy on Carbon as a High-Performance DMFC Catalyst. *Chem. Mater.* **2006**, *18*, 4209−4211.
(57) Yan, S. C.; Li, Z. S.; Zou, Z. G. Photodegradation Performance of g-C_3N_4 Fabricated by Directly Heating Melamine. *Langmuir* **2009**, *25*, 10397−10401.
(58) Wang, X.; Chen, X.; Thomas, A.; Fu, X.; Antonietti, M. Metal-Containing Carbon Nitride Compounds: A New Functional Organic-Metal Hybrid Material. *Adv. Mater.* **2009**, *21*, 1609−1612.
(59) Sun, B.-w.; Yu, H.-y.; Yang, Y.-j.; Li, H.-j.; Zhai, C.-y.; Qian, D.-J.; Chen, M. New complete assignment of X-ray powder diffraction patterns in graphitic carbon nitride using discrete Fourier transform and direct experimental evidence. *Phys. Chem. Chem. Phys.* **2017**, *19*, 26072−26084.
(60) Kulkarni, R.; Kunwar, S.; Mandavkar, R.; Jeong, J.-H.; Lee, J. Hydrogen Peroxide Detection by Super-Porous Hybrid CuO/Pt NP Platform: Improved Sensitivity and Selectivity. *Nanomaterials* **2020**, *10*, No. 2034.
(61) Lu, X.; Tan, T. H.; Ng, Y. H.; Amal, R. Highly Selective and Stable Reduction of CO_2 to CO by a Graphitic Carbon Nitride/Carbon Nanotube Composite Electrocatalyst. *Chem. - Eur. J.* **2016**, *22*, 11991−11996.
(62) Kim, D.; Kley, C. S.; Li, Y.; Yang, P. Copper Nanoparticle Ensembles for Selective Electroreduction of CO_2 to C2−C3 Products. *Proc. Natl. Acad. Sci. U.S.A.* **2017**, *114*, 10560−11056.
(63) Reske, R.; Mistry, H.; Behafarid, F.; Cuenya, B. R.; Strasser, P. Particle Size Effects in the Catalytic Electroreduction of CO_2 on Cu Nanoparticles. *J. Am. Chem. Soc.* **2014**, *136*, 6978−6986.
(64) Singh, A. K.; Yasri, N.; Karan, K.; Roberts, E. P. L. Electrocatalytic Activity of Functionalized Carbon Paper Electrodes and Their Correlation to the Fermi Level Derived from Raman Spectra. *ACS Appl. Energy Mater.* **2019**, *2*, 2324−2336.
(65) Lee, S. H.; Lin, J. C.; Farmand, M.; Landers, A. T.; Feaster, J. T.; Acosta, J. E. A.; Beeman, J. W.; Ye, Y.; Yano, J.; Mehta, A.; Davis, R. C.; Jaramillo, T. F.; Hahn, C.; Drisdell, W. S. Oxidation State and Surface Reconstruction of Cu under CO_2 Reduction Conditions from *in Situ* X-Ray Characterization. *J. Am. Chem. Soc.* **2021**, *143*, 588−592.
(66) Möller, T.; Scholten, F.; Thanh, T. N.; Sinev, I.; Timoshenko, J.; Wang, X.; Jovanov, Z.; Gliech, M.; Cuenya, B. R.; Varela, A. S.; Strasser, P. Electrocatalytic CO_2 reduction on CuO_x nanocubes: Tracking the evolution of chemical state, geometric structure, and

catalytic selectivity using operando spectroscopy. *Angew. Chem., Int. Ed.* **2020**, *59*, 17974−17983.

(67) Wang, X.; Varela, A. S.; Bergmann, A.; Kühl, S.; Strasser, P. Catalyst Particle Density Controls Hydrocarbon Product Selectivity in CO_2 Electroreduction on CuOx. *ChemSusChem* **2017**, *10*, 4642−4649.

(68) Peterson, A. A.; Abild-Pedersen, F.; Studt, F.; Rossmeisl, J.; Nørskov, J. K. How Copper Catalyzes the Electroreduction of Carbon Dioxide into Hydrocarbon Fuels. *Energy Environ. Sci.* **2010**, *3*, 1311−1315.

(69) Zhang, H.; Chang, X.; Chen, J. G.; Goddard, W. A., III; Xu, B.; Cheng, M. J.; Lu, Q. Computational and experimental demonstrations of one-pot tandem catalysis for electrochemical carbon dioxide reduction to methane. *Nat. Commun.* **2019**, *10*, No. 3340.

(70) Mangione, G.; Huang, J.; Buonsanti, R.; Corminboeuf, C. Dual-Facet Mechanism in Copper Nanocubes for Electrochemical CO_2 Reduction into Ethylene. *J. Phys. Chem. Lett.* **2019**, *10*, 4259−4265.

(71) Todorova, T. K.; Schreiber, M. W.; Fontecave, M. Mechanistic Understanding of CO_2 Reduction Reaction (CO_2RR) Toward Multicarbon Products by Heterogeneous Copper-Based Catalysts. *ACS Catal.* **2020**, *10*, 1754−1768.

(72) Chang, C.-C.; Ku, M.-S. Role of High-Index Facet Cu(711) Surface in Controlling the C_2 Selectivity for CO_2 Reduction Reaction - A DFT Study. *J. Phys. Chem. C* **2021**, *125*, 10919−10925.

https://doi.org/10.1021/acsomega.2c05513
ACS Omega 2023, 8, 7368−7377